

# Monolithic Photoelectrochemical Device for Direct Water Splitting with 19% Efficiency

Wen-Hui Cheng,<sup>†,‡</sup> Matthias H. Richter,<sup>‡,§</sup> Matthias M. May,<sup>\*,||,⊥,‡</sup> Jens Ohlmann,<sup>▽</sup> David Lackner,<sup>▽</sup> Frank Dimroth,<sup>▽</sup> Thomas Hannappel,<sup>\*,#</sup> Harry A. Atwater,<sup>\*,†,‡,⊙</sup> and Hans-Joachim Lewerenz<sup>‡,⊙</sup>

<sup>†</sup>Department of Applied Physics and Material Science, California Institute of Technology, Pasadena, California 91125, United States

<sup>‡</sup>Joint Center for Artificial Photosynthesis, California Institute of Technology, Pasadena, California 91125, United States

<sup>§</sup>Division of Chemistry and Chemical Engineering, California Institute of Technology, Pasadena, California 91125, United States

<sup>||</sup>Department of Chemistry, University of Cambridge, CB2 1EW Cambridge, United Kingdom

<sup>⊥</sup>Helmholtz-Zentrum Berlin für Materialien und Energie GmbH, Institute for Solar Fuels, D-14109 Berlin, Germany

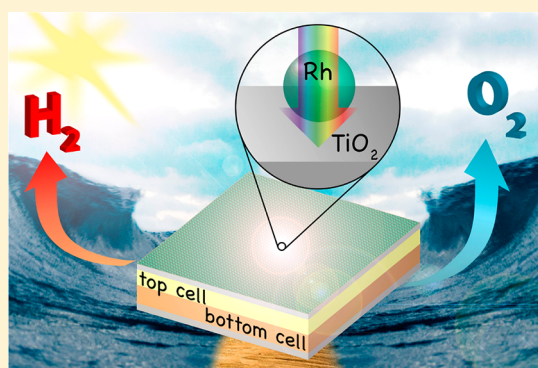
<sup>#</sup>Department of Physics, Technische Universität Ilmenau, D-98693 Ilmenau, Germany

<sup>▽</sup>Fraunhofer Institute for Solar Energy Systems ISE, D-79110 Freiburg, Germany

<sup>⊙</sup>Division of Engineering and Applied Science, California Institute of Technology, Pasadena, California 91125, United States

## S Supporting Information

**ABSTRACT:** Efficient unassisted solar water splitting, a pathway to storable renewable energy in the form of chemical bonds, requires optimization of a photoelectrochemical device based on photovoltaic tandem heterojunctions. We report a monolithic photocathode device architecture that exhibits significantly reduced surface reflectivity, minimizing parasitic light absorption and reflection losses. A tailored multifunctional crystalline titania interphase layer acts as a corrosion protection layer, with favorable band alignment between the semiconductor conduction band and the energy level for water reduction, facilitating electron transport at the cathode–electrolyte interface. It also provides a favorable substrate for adhesion of high-activity Rh catalyst nanoparticles. Under simulated AM 1.5G irradiation, solar-to-hydrogen efficiencies of 19.3 and 18.5% are obtained in acidic and neutral electrolytes, respectively. The system reaches a value of 0.85 of the theoretical limit for photoelectrochemical water splitting for the energy gap combination employed in the tandem-junction photoelectrode structure.



Electrochemical water splitting was achieved by van Trostwijk and Deiman in 1789 and, about a decade later, by Nichol森 and Carlisle,<sup>1,2</sup> whereas light-induced unassisted water splitting with rutile as a photoanode was reported in 1972, resulting in a small but measurable efficiency.<sup>3</sup> Efficient solar water splitting was first achieved using a dual-junction tandem photoelectrode<sup>4</sup> under a light intensity equivalent to 11 suns.

In 2015, several devices with solar-to-hydrogen (STH) efficiency greater than 10% at 1 sun illumination were reported,<sup>5</sup> and in 2017, an efficiency of 16.2% was achieved.<sup>6</sup> Overall, advances in solar water splitting<sup>1</sup> have led to a number of functional prototypes of photoelectrochemical and photoelectrosynthetic cells in recent years,<sup>2</sup> featuring improved photoelectrode stability through the use of corrosion protection layers.<sup>7,8</sup> However, comparison of STH efficiencies realized so far with theoretical limiting efficiencies<sup>9</sup> shows considerable room for further improvement; at present, the

highest-efficiency systems reach about 2/3 of the theoretical limiting value for a given photoelectrode. To enable STH efficiencies approaching theoretical limits, the photovoltage has to be as large as possible, which requires a minimized photoelectrode dark current. This in turn dictates that the charge carrier recombination at interfaces must be prevented. To maximize the photocurrent, a reduction of the photoelectrode surface reflectivity under operating conditions is also required, as is mitigation of light absorption in the catalyst layer applied to the photoelectrode surface.<sup>10</sup>

If one utilizes the band gap combination of a given tandem photoelectrode and the best reported exchange current densities for the hydrogen evolution reaction (HER) and oxygen evolution reaction (OER) and omits losses due to

Received: June 2, 2018

Accepted: June 25, 2018

Published: June 25, 2018

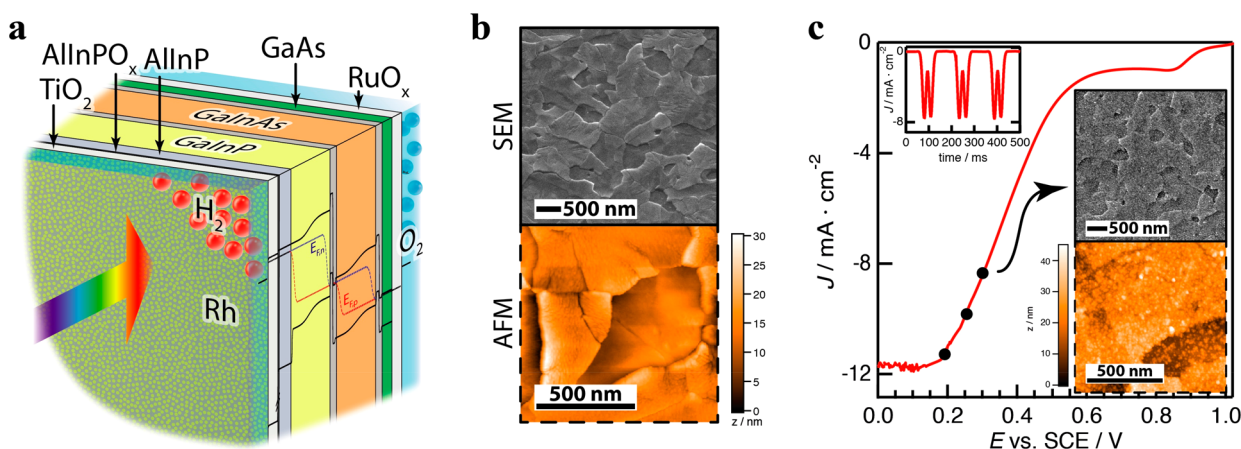


**Figure 1.** Functionalization of a dual-junction tandem as the photoelectrode for unassisted water splitting: (a) schematic of the device structure after functionalization with interfacial films and electrocatalysts (see text); (b) topography of the crystalline anatase  $\text{TiO}_2$  layer by HRSEM and AFM; (c) protocol of the photoelectrodeposition of Rh NPs; the arrow shows the potential used for stroboscopic deposition under white light illumination, as shown in the upper left inset. The potential choices made are indicated by black dots; the best result was obtained for  $E = +0.3$  V vs SCE. Resulting Rh particles are shown in the inset under the  $J$ - $V$  characteristic (upper image: SEM; lower one: AFM). The potential control and corresponding particle size distribution are included in Supporting Information section S1. The root-mean-square surface roughness of  $\text{TiO}_2$  is 6.3 and 3.6 nm (with/without Rh, respectively).

external radiative efficiency (ERE) defined as the portion of radiative recombination to the total (radiative and non-radiative) recombination and solution resistance, the realistic limiting STH efficiencies can be calculated.<sup>9</sup> For the tandem photoelectrode used here (see Supporting Information section S1), this value is 22.8%. Approaching such limiting efficiencies provides a clear objective for a renewable fuels technology because inclusion of hydrogen in the existing worldwide fuel generation infrastructure could enable direct and widespread application of renewable fuels in the transportation sector and for electricity generation.<sup>11</sup>

Here, we demonstrate an approach to achieving efficiencies near the theoretical limits for the photoelectrode energy band gaps employed. A key aspect of our approach is (i) the use of a crystalline anatase  $\text{TiO}_2$  photocathode interfacial layer (see Supporting Information section S3), deposited by atomic layer deposition (ALD), to facilitate reduced reflectivity and interface recombination velocity and (ii) a size distribution and spatial arrangement of Rh catalyst nanoparticles (NPs) tailored to achieve ultralow light attenuation. The crystalline anatase  $\text{TiO}_2$  interlayer shows excellent energy band alignment with the tandem window layer and its interfacial ultrathin oxidized surface part and with the electrolyte. In addition, it serves as an efficient antireflection coating and as a support for the catalyst NPs, with enhanced adhesion relative to III-V compound semiconductor surfaces.

We employ a dual-junction tandem photoelectrode where the high-band-gap subcell thickness has been increased for better current matching and the transparency of the tunnel diode was improved.<sup>10,12,13</sup> To further increase the STH efficiency, interfacial layers have been designed to reduce charge carrier recombination and to increase optical light coupling into the photoelectrode absorber layers. The surface conditioning sequence resulted in etching of the GaAs cap layer by an  $\text{NH}_4\text{OH}-\text{H}_2\text{O}_2-\text{H}_2\text{O}$  solution, leaving an oxidized surface layer ( $\text{AlInPO}_x$ ) on top of the  $n^+$ -doped  $\text{AlInP}$  window layer (see Supporting Information section S1). A crystalline anatase  $\text{TiO}_2$  film with an effective thickness of 30 nm was deposited to act as a corrosion protection layer and an antireflection coating, as well as serving as a conducting

substrate surface for photoelectrodeposition of Rh NP electrocatalysts. The Rh NPs exhibited large surface areas and thus high exchange current and, simultaneously, particularly low light attenuation. The photocathode device configuration employed is generally less prone to photo-decomposition than photoanode devices, where charge carriers with high oxidation potential are present at the semiconductor surface. Figure 1 shows a schematic of the resulting device: the photoelectrode consisting of GaInP and GaInAs subcells on a GaAs substrate, an anatase  $\text{TiO}_2$  protective layer, the Rh NP catalyst layer, and a sputtered  $\text{RuO}_2$  counter electrode (OER) are depicted. Also depicted on the side of the layer structure in Figure 1 is an energy band diagram under illumination where the quasi-Fermi levels show the splitting for electrons and holes necessary to achieve unassisted water splitting (see Supporting Information section S4). The surface of the crystalline  $\text{TiO}_2$  film illustrated in Figure 1b indicates a continuous film with height variations, seen by AFM, that give it a flake-like appearance. Figure 1c illustrates the protocol for pulsed photoelectrodeposition of Rh catalyst NPs (see Supporting Information section S1), and the inset gives SEM and AFM images of the Rh NPs. Figure 1c depicts the procedure to obtain the highest-activity catalysts at almost negligible light attenuation; fine control of particle size smaller than 20 nm was achieved by careful adjustment of the electrode potential, enabling considerably higher catalyst loading compared to that of a dense film of equivalent catalyst loading deposited by conventional vapor-phase or electrochemical reduction. This procedure facilitates photocathodes with high-transparency catalysts, which maintain high photocurrent densities and result in increased efficiency, which is determined from the relation

$$\eta_{\text{STH}} = \frac{J_{\text{op}} \cdot E_{\text{rxn}} \cdot f_{\text{FE}}}{P_{\text{in}}} \quad (1)$$

The solar fuel generator efficiency  $\eta_{\text{STH}}$  is given by the operating current at the counter electrode potential, the thermodynamic value for the reaction ( $E_{\text{rxn}} = 1.23$  V for water splitting under standard conditions), and the reaction Faradaic

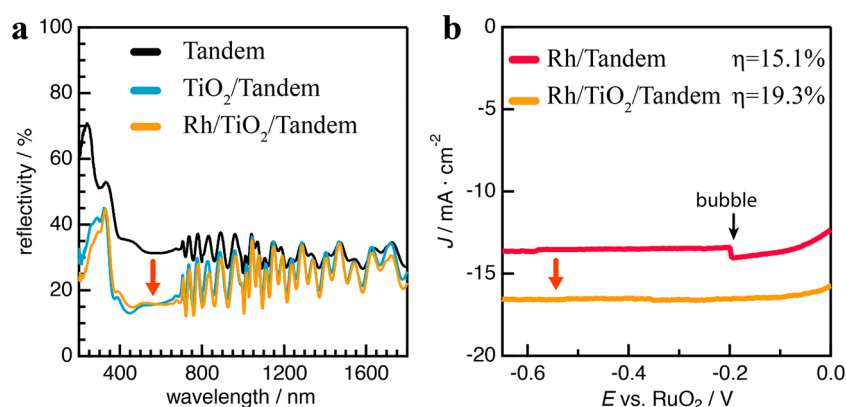


Figure 2. Optoelectronic properties of the surface-functionalized electrolyte/Rh/TiO<sub>2</sub>/oxide/AlInP–GaInP/GaInAs/GaAs water splitting device; (a) reflectivity  $R_a$ , measured in air, of the dual-junction tandem solar cell without ARC (black curve) and second reflectivity obtained after TiO<sub>2</sub> coating (blue curve) and after photoelectrochemically deposited Rh NPs (yellow curve);  $R_a$  is larger than that under operation in electrolyte due to the different refractive indices of air and water; (b) comparison of the output characteristics of the tandem device after cap layer etching and of the full surface-functionalized photoelectrode. The orange arrows indicate the improvement after incorporation of the TiO<sub>2</sub> layer.

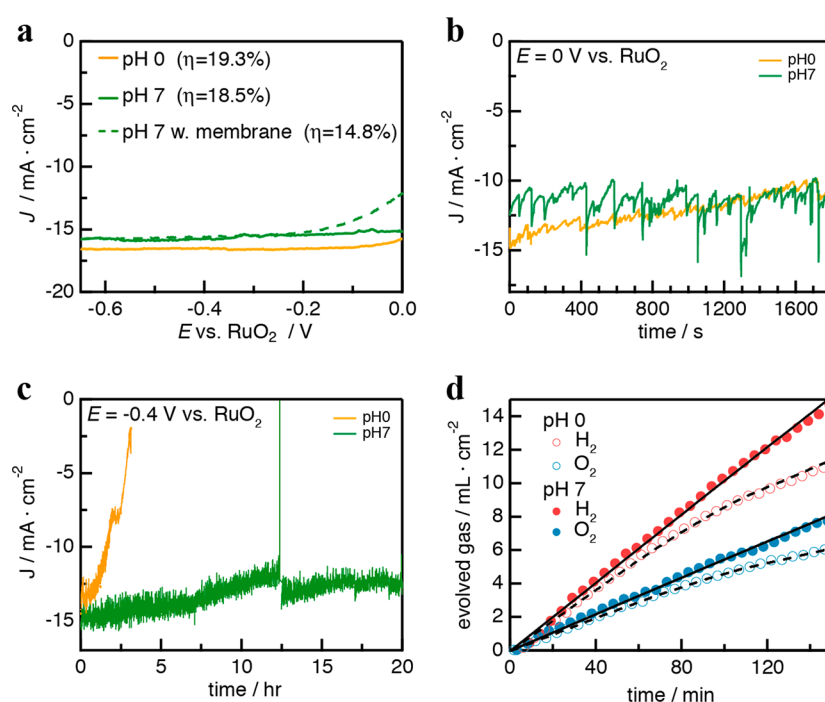


Figure 3. Output characteristics of the RuO<sub>2</sub>–GaAs/GaInAs/GaInP/AlInP–anatase TiO<sub>2</sub>–Rh/electrolyte dual-junction tandem structure: (a) photocurrent–voltage characteristics in acidic (pH 0) and neutral (pH 7) electrolyte and in neutral electrolyte including an AEM membrane; (b) chronoamperometric data of the initial temporal regime; (c) stability measurements at  $-0.4$  V vs a RuO<sub>2</sub> counter electrode for acidic and neutral pH; (d) hydrogen and oxygen gas collection for operation in acidic (open spheres) and neutral (full spheres) electrolyte. The measured gas volume for oxygen (blue symbols) and hydrogen (red symbols) is overlaid with the expected produced gas volume, as calculated from charge passed through the anode and cathode.

efficiency  $f_{FE}$  determined by gas product analysis measurements.

Electronically, the photoelectrode configuration used here facilitates alignment of the conduction bands of the AlInP window layer of the tandem photoelectrode to the indium oxide and indium phosphate layers (created by the cap layer etching process) and the anatase TiO<sub>2</sub> protection/antireflective layer. We note that photogenerated electrons, which are minority carriers in the main part of the tandem subcells, become majority carriers in the AlInP and TiO<sub>2</sub> layers, reducing recombination losses in carrier transport. Details of

the energy band alignment and the photoelectron spectroscopy and optical data used to support it are described in the [Supporting Information section S4](#). In addition, the large valence band offset between AlInP and TiO<sub>2</sub> blocks interfacial hole transport, resulting in a small overall reverse saturation current, improving the photovoltage. This feature is important for achieving high STH efficiencies.

The influence of the surface modifications on optical properties and on the photocurrent is shown in [Figure 2](#). A reduction of the reflectivity by  $\sim 15\%$  is achieved by use of the TiO<sub>2</sub> interlayer ([Supporting Information section S5](#)), whereas



the Rh NPs in Figure 2a show negligible additional absorption, which is attributed to the blue-shifted plasmonic resonance of the Rh NPs. For particle sizes below 20 nm, a shift from the visible region into the ultraviolet one occurs, making the Rh layer almost fully transparent.<sup>14–16</sup> The detailed optimization of the optical design regarding the thickness of TiO<sub>2</sub> and Rh particle size is discussed in Supporting Information section S6 including both simulations and experimental support.

The corresponding photocurrent–voltage characteristics in acidic electrolyte demonstrate a pronounced increase in the current and, as expected, also a shift of the bend of the photocurrent characteristic toward more anodic potentials, thereby additionally increasing the photocurrent at the RuO<sub>2</sub> counter electrode (OER) potential. The result with incorporation of TiO<sub>2</sub> is a relative increase of 28% of the tandem cell output. A STH efficiency of 19.3% is obtained at 0 V, with an operating current of 15.7 mA/cm<sup>2</sup>, assuming an initial Faradaic efficiency of unity, which is supported by the gas evolution measurements shown in Figure 3b. These data represent a 20% increase in efficiency above the previously reported 1 sun photoelectrosynthetic cell efficiency benchmark.<sup>6</sup>

The high photocurrent at 0 V vs RuO<sub>2</sub> indicates that electron transport is virtually uninhibited from the absorber layer through the indium and phosphorus oxide and TiO<sub>2</sub> interfacial layers to the electrolyte. The corresponding energy band relations can be inferred from surface characterization using ultraviolet and X-ray photoelectron spectroscopy. While the simplest approach to assessment of band alignment follows Anderson's idealized model<sup>17</sup> for planar contacts and does not consider energy band shifts due to surface and/or interface dipoles, this approach certainly does not apply here as the junctions formed at the AlInP/oxide, oxide/TiO<sub>2</sub>, and TiO<sub>2</sub>/Rh/electrolyte interfaces are complex. Thus, the energy band diagram of the heterojunction structure was inferred from ultraviolet and X-ray photoelectron spectroscopy measurements and can be found in the Supporting Information section S4. It should be noted that equilibrium formation between small metallic catalyst NPs and semiconductors appears to depend on the substrate doping level<sup>5</sup> and obviously does not follow a Schottky thermionic emission model, in particular, in contact with an electrolyte.<sup>18,19</sup> In addition, metal work functions depend on NP size;<sup>20</sup> therefore, comparison of the energy levels of NP catalyst layers with planar thin films is notably challenging; therefore, only an estimate of the NP catalyst layer energy level can be given, supported by the device operating data.

The output data shown in Figure 2b were obtained in an acidic electrolyte of pH 0. Figure 3 summarizes the main performance characteristics. Figure 3a illustrates the photocurrent–voltage characteristics under three conditions: (i) at pH 0 with 19.3% STH, (ii) at neutral pH with 18.5% STH, and (iii) using an anion exchange membrane (AEM) with a STH of 14.8%. The observed unassisted water splitting efficiencies critically depend on the experimental conditions (details about the efficiency benchmarking of our PEC device under AM 1.5G conditions, as well as a discussion of efficiency accuracy and polarization loss, are given in the Supporting Information section S7).

Figure 3b gives the unassisted two-electrode photocurrent density vs time for the initial operation regime, showing that while the photocurrent density decreases with time for acidic pH it remains more stable in neutral pH solutions. Chronoamperometric tests (at −0.4 V vs counter electrode,

as shown in Figure 3c) show that the device photocurrent density decreases in an acidic electrolyte to low values within 3 h. However, in neutral pH electrolyte, stability over 20 h was demonstrated, with the photocurrent density remaining at 83% of its initial value (see comparative PEC test conditions and results in the Supporting Information section S8). In both cases, for pH 0 and 7, near-unity Faradaic efficiency is confirmed through the agreement between the expected (solid line) and measured gas volumes (symbols) in Figure 3d. However, whereas the curves for pH 7 stay linear with a constant gas production rate for H<sub>2</sub>/O<sub>2</sub>, as expected from the stability measurements, the curves for pH 0 show a deviation from linearity due to the decreasing photocurrent.

Etching of TiO<sub>2</sub> is expected to occur at pH 0 but not at pH 7, as can be seen in the TiO<sub>2</sub> Pourbaix diagram in Supporting Information section S10. Corrosion reactions can degrade the junction photovoltage, as well as lead to undercutting and removal of catalyst particles, thus reducing the exchange current of the Rh NP arrangement and slowing of the HER kinetics. The system reacts also sensitively to series resistance changes, as illustrated by characteristics for devices employing an anion exchange membrane. The bend of the *J*–*V* curve is shifted to cathodic potentials. However, device operation at pH 7 still yields a high STH efficiency of 18.5% and the device appears to be stable for a more extended period, in accordance with predictions of TiO<sub>2</sub> stability from thermodynamics. Even a slower reduction of the photocurrent is observed; we found that this photocurrent reduction could be partially reversed by immersion of the device from the electrolyte solution and applying a soft cleansing procedure (see Supporting Information section S8). The observation that the photocurrent can be partially restored appears to rule out loss of Rh catalyst particles or even partial removal of the anatase interfacial layer as causes of photocurrent reduction. We find, however, that the surface chemistry of Rh is influenced by the phosphate buffer of the neutral electrolyte; XPS in Supporting Information section S10 clearly indicates PO<sub>4</sub> formation on the Rh surfaces because of the absence of an In signal, which would have been observed in case of InPO<sub>x</sub> formation, concurrent with corrosion of the absorber. The photoelectrode regeneration procedure results in a 50% recovery of the photocurrent lost during the first 12 h, suggesting that the high porosity of the Rh NP layer inhibits full recovery by short intermediate treatment. Employing a different electrolyte for pH 7 conditions might therefore benefit long-term activity of the device. (see details in Supporting Information section S10).

Increasing the efficiency of a photoelectrosynthetic device from already high values toward theoretical limits is especially challenging. We have used a series of surface conditioning steps that have a two-fold function: light management was drastically improved and the electronic properties were at least maintained. Compared to our earlier results,<sup>5</sup> we see an increase in the available cell voltage that is related to the increase in photocurrent at the counter electrode operation potential. Junction formation between the etched AlInP layer, TiO<sub>2</sub> layer, and Rh NPs suggests that the Fermi level alignment is nearly ideal.

Figure 4 shows a summary to date of selected STH efficiencies realized for monolithic integrated photoelectrosynthetic devices capable of unassisted water splitting.

Using the parameters shown in Table 1, our photoelectrosynthetic device reaches 0.85 of the theoretical limiting efficiency. It should be noted that the theoretical efficiency

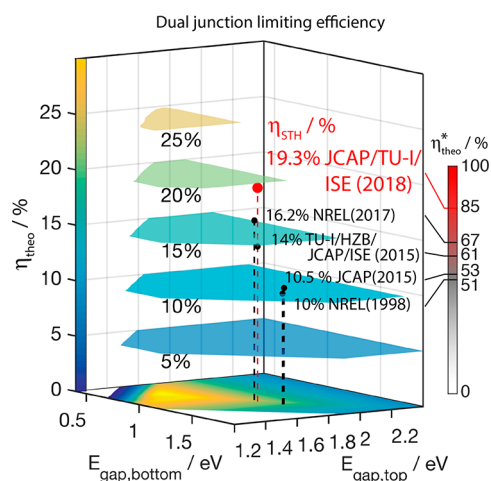


**Figure 4.** Comparison of realized limiting STH efficiencies and historic development. The analysis refers to a theoretical benchmarking value  $\eta_{\text{theo}}$  (see text) and takes into account the top and bottom cell band gaps for the respective photolysis cells; also shown are the institutions of the contributing research teams. Abbreviations: NREL - National Renewable Energy Laboratory, USA; ISE - Institute for Solar Energy, Germany; JCAP - Joint Center for Artificial Photosynthesis, Caltech; TU-I - Ilmenau University of Technology, Germany; HZB - Helmholtz Zentrum Berlin, Germany. The bar chart on the right indicates the achieved efficiency with respect to the respective theoretical limit ( $\eta_{\text{theo}}^*$ ). See detail values in [Supporting Information section S10](#).

**Table 1.** Approaches to Theoretical Limitation of Light-Induced Photoelectrochemical Water Splitting<sup>a</sup>

	$J_{0,\text{cathode}}$ [mA cm <sup>-2</sup> ]	$J_{0,\text{anode}}$ [mA cm <sup>-2</sup> ]	$f_{\text{abs}}$	ERE	$R_s$ [Ω]	$R_{\text{sh}}$ [Ω]
ideal	∞	∞	1	1	0	∞
$J_{\text{XC}}$ limited	1	10 <sup>-3</sup>	1	1	0	∞
$J_{\text{XC}}$ and optically limited	1	10 <sup>-3</sup>	0.9	0.03	0	∞

<sup>a</sup>Ideal: only exchange current density-limited and devices that are optically and electrochemically limited are displayed in rows 1–3, respectively. For the used band gap combination and only catalytic exchange current density ( $J_{\text{XC}}$ ) limitation,  $\eta_{\text{theo}} = 22.8\%$  at AM 1.5G irradiation.

determined from the data in [Table 1](#) is based on the best presently known electrocatalysts, a unity photoelectrode radiative efficiency, and an absence of absorption losses.<sup>9</sup> We also calculated the STH efficiency as a function of Tafel slope, exchange current density, and ohmic drop to evaluate whether the optical or the electrochemical polarization losses dominate the solar cell performance (see [Supporting Information section S7](#), Figure S17). Our record device is located in the region of highest efficiency, showing that the optical loss is the limiting factor. However, the system, in principle, reacts sensitively to the polarization losses, emphasizing the importance of judiciously combining the interface and catalyst.

Stability appears to remain an issue of this photocathode device configuration, but we have demonstrated high efficiency in neutral electrolytes and that extended operation of photocathode devices becomes possible if one can control the Rh surface chemistry. The use of Rh NPs with tailored size and shape distributions enables ultralow absorption. The future design of even more optimized tandem photoelectrodes

appears to be possible, enabling solar fuel generation (water splitting as well as CO<sub>2</sub> or N<sub>2</sub> reduction) efficiencies to be even higher than those reported here, for example, with STH champion device efficiencies of >20% for integrated direct water photolysis being a realistic goal.

## ■ ASSOCIATED CONTENT

### Supporting Information

The Supporting Information is available free of charge on the [ACS Publications website](#) at DOI: [10.1021/acsenenergylett.8b00920](https://doi.org/10.1021/acsenenergylett.8b00920).

Device fabrication; materials characterization techniques; TiO<sub>2</sub> characterization; surface layer band alignment; absorption enhancement by TiO<sub>2</sub>; optimization of the optical design; assessment of the solar-to-hydrogen efficiency measurement; comparative PEC test conditions and results; surface tension variation between pH 0 and 7; X-ray photoelectron spectra and mechanism development; and STH benchmarks ([PDF](#))

## ■ AUTHOR INFORMATION

### Corresponding Authors

\*E-mail: [haa@caltech.edu](mailto:haa@caltech.edu) (H.A.A.).

\*E-mail: [thomas.hannappel@tu-ilmenau.de](mailto:thomas.hannappel@tu-ilmenau.de) (T.H.).

\*E-mail: [matthias.may@physik.hu-berlin.de](mailto:matthias.may@physik.hu-berlin.de) (M.M.M.).

### ORCID

Harry A. Atwater: 0000-0001-9435-0201

### Author Contributions

T.H., H.J.L., M.M.M., W.H.C., M.H.R. and H.A.A. conceived of the experimental study. W.H.C. and M.H.R. executed the experiments and did the data analysis. J.O., D.L., and F.D. prepared the tandem absorber. W.H.C., M.H.R., H.J.L., and H.A.A. wrote the paper, and all authors commented on the manuscript.

### Notes

The authors declare no competing financial interest.

## ■ ACKNOWLEDGMENTS

The authors acknowledge Katherine T. Fountaine for the calculation of theoretical photocurrent efficiencies of 2J PEC devices. This work was supported through the Office of Science of the U.S. Department of Energy (DOE) under Award No. DE SC0004993 to the Joint Center for Artificial Photosynthesis, a DOE Energy Innovation Hub. Research was in part carried out at the Molecular Materials Research Center of the Beckman Institute of the California Institute of Technology. The work on tandem absorbers was funded by the German Federal Ministry of Education and research (BMBF) under Contract Number FKZ 03F0432A (HyCon). M.M.M. acknowledges funding from the fellowship programme of the German National Academy of Sciences Leopoldina, Grant LPDS 2015-09.

## ■ REFERENCES

- (1) Walter, M. G.; Warren, E. L.; McKone, J. R.; Boettcher, S. W.; Mi, Q.; Santori, E. A.; Lewis, N. S. Solar Water Splitting Cells. *Chem. Rev.* **2010**, *110*, 6446–6473.
- (2) Xiang, C.; Weber, A. Z.; Ardo, S.; Berger, A.; Chen, Y.; Coridan, R.; Fountaine, K. T.; Haussener, S.; Hu, S.; Liu, R.; et al. Modeling, Simulation, and Implementation of Solar-Driven Water-Splitting Devices. *Angew. Chem., Int. Ed.* **2016**, *55*, 12974–12988.

- (3) Fujishima, A.; Honda, K. Electrochemical Photolysis of Water at a Semiconductor Electrode. *Nature* **1972**, *238*, 37–38.
- (4) Khaselev, O.; Turner, J. A. A Monolithic Photovoltaic-Photoelectrochemical Device for Hydrogen Production via Water Splitting. *Science* **1998**, *280*, 425–427.
- (5) May, M. M.; Lewerenz, H. J.; Lackner, D.; Dimroth, F.; Hannappel, T. Efficient Direct Solar-to-Hydrogen Conversion by in Situ Interface Transformation of a Tandem Structure. *Nat. Commun.* **2015**, *6*, 8286.
- (6) Young, J. L.; Steiner, M. A.; Döschner, H.; France, R. M.; Turner, J. A.; Deutsch, T. G. Direct Solar-to-Hydrogen Conversion via Inverted Metamorphic Multi-Junction Semiconductor Architectures. *Nature Energy* **2017**, *2*, 17028.
- (7) Lichterman, M. F.; Sun, K.; Hu, S.; Zhou, X.; McDowell, M. T.; Shaner, M. R.; Richter, M. H.; Crumlin, E. J.; Carim, A. I.; Saadi, F. H.; et al. Protection of Inorganic Semiconductors for Sustained, Efficient Photoelectrochemical Water Oxidation. *Catal. Today* **2016**, *262*, 11–23.
- (8) Bae, D.; Pedersen, T.; Seger, B.; Iandolo, B.; Hansen, O.; Vesborg, P. C. K.; Chorkendorff, I. Carrier-Selective P- and N-Contacts for Efficient and Stable Photocatalytic Water Reduction. *Catal. Today* **2017**, *290*, 59–64.
- (9) Fountaine, K. T.; Lewerenz, H. J.; Atwater, H. A. Efficiency Limits for Photoelectrochemical Water-Splitting. *Nat. Commun.* **2016**, *7*, 13706.
- (10) May, M. M.; Lackner, D.; Ohlmann, J.; Dimroth, F.; van de Krol, R.; Hannappel, T.; Schwarzburg, K. On the Benchmarking of Multi-Junction Photoelectrochemical Fuel Generating Devices. *Sustainable Energy Fuels* **2017**, *1*, 492–503.
- (11) Sathre, R.; Scown, C. D.; Morrow, W. R.; Stevens, J. C.; Sharp, I. D.; Ager, J. W., III; Walczak, K. A.; Houle, F. A.; Greenblatt, J. B. Life-Cycle Net Energy Assessment of Large-Scale Hydrogen Production via Photoelectrochemical Water Splitting. *Energy Environ. Sci.* **2014**, *7*, 3264–3278.
- (12) Dimroth, F.; Beckert, R.; Meusel, M.; Schubert, U.; Bett, A. W. Metamorphic  $\text{GaIn}_{1-y}\text{P}/\text{Ga}_{1-x}\text{In}_x\text{As}$  Tandem Solar Cells for Space and for Terrestrial Concentrator Applications at  $C > 1000$  Suns. *Prog. Photovoltaics* **2001**, *9*, 165–178.
- (13) Ohlmann, J.; Sanchez, J. F. M.; Lackner, D.; Förster, P.; Steiner, M.; Fallisch, A.; Dimroth, F. Recent Development in Direct Generation of Hydrogen Using Multi-Junction Solar Cells. *AIP Conf. Proc.* **2016**, *1766*, 080004.
- (14) Porter, J. D.; Heller, A.; Aspnes, D. E. Experiment and Theory of “Transparent” Metal Films. *Nature* **1985**, *313*, 664–666.
- (15) Degani, Y.; Sheng, T. T.; Heller, A.; Aspnes, D. E.; Studna, A. A.; Porter, J. D. “Transparent” Metals: Preparation and Characterization of Light-Transmitting Palladium, Rhodium, and Rhenium Films. *J. Electroanal. Chem. Interfacial Electrochem.* **1987**, *228*, 167–178.
- (16) Sanz, J. M.; Ortiz, D.; Alcaraz de la Osa, R.; Saiz, J. M.; González, F.; Brown, A. S.; Losurdo, M.; Everitt, H. O.; Moreno, F. UV Plasmonic Behavior of Various Metal Nanoparticles in the Near- and Far-Field Regimes: Geometry and Substrate Effects. *J. Phys. Chem. C* **2013**, *117*, 19606–19615.
- (17) Anderson, R. L. Germanium-Gallium Arsenide Heterojunctions. *IBM J. Res. Dev.* **1960**, *4*, 283–287.
- (18) Skorupska, K.; Pettenkofer, C.; Sadewasser, S.; Streicher, F.; Haiss, W.; Lewerenz, H. J. Electronic and Morphological Properties of the Electrochemically Prepared Step Bunched Silicon (111) Surface. *Phys. Status Solidi B* **2011**, *248*, 361–369.
- (19) Rizk, R.; de Mierry, P.; Ballutaud, D.; Aucouturier, M.; Mathiot, D. Hydrogen Diffusion and Passivation Processes in P- And N-Type Crystalline Silicon. *Phys. Rev. B: Condens. Matter Mater. Phys.* **1991**, *44*, 6141–6151.
- (20) Zhang, Y.; Pluchery, O.; Caillard, L.; Lamic-Humblot, A.-F.; Casale, S.; Chabal, Y. J.; Salmeron, M. B. Sensing the Charge State of Single Gold Nanoparticles via Work Function Measurements. *Nano Lett.* **2015**, *15*, 51–55.